Application of Multiplicative Regularization to the Finite-Element Contrast Source Inversion Method

Amer Zakaria and Joe LoVetri

***Abstract*—Multiplicative regularization is applied to the finite-element contrast source inversion (FEM-CSI) algorithm recently developed for microwave tomography. It is described for the two-dimensional (2D) transverse-magnetic (TM) case and tested by inverting experimental data where the fields can be approximated as TM. The unknown contrast, which is to be reconstructed, is represented using nodal variables and first-order basis functions on triangular elements; the same first-order basis functions used in the FEM solution of the accompanying field problem. This approach is different from other MR-CSI implementations where the contrast variables are located on a uniform grid of rectangular cells and represented using pulse basis functions. The linear basis function representation of the contrast makes it difficult to apply the weighted L_2-norm total variation multiplicative regularization which requires that gradient and divergence operators be applied to the predicted contrast at each iteration of the inversion algorithm; the use of finite-difference operators for this purpose becomes unwieldy. Thus, a new technique is introduced to perform these operators on the triangular mesh.**

***Index Terms*—Contrast source inversion, finite-element method, microwave tomography, multiplicative regularization.**

I. Introduction

In microwave tomography (MWT), an object of interest (OI) is illuminated by several electromagnetic sources and data are collected at different receiver locations for the purpose of quantitatively imaging the dielectric properties of the OI. The associated nonlinear inverse scattering problem is here formulated as a minimization of the least-squares error between the collected data and a scattering model which is a function of the variables used to discretize the dielectric contrast. Various local optimization algorithms are available to perform the minimization, e.g., Gauss-Newton inversion (GNI) and the contrast source inversion (CSI), but the ill-posedness of the electromagnetic inverse scattering problem requires that some form of regularization be explicitly, or implicitly, applied.

Different regularization methods have been reported in the literature and have been successfully applied for various applications [1]. A successful regularization technique which has been used is the weighted L_2-norm total variation multiplicative regularization (MR), which has been incorporated into both GNI and CSI [2]–[9]. Not only has it been shown to enhance the outcome of the inversion algorithm, i.e., regularize the optimization, but it also has other desirable features: (*i*) its edge-preserving characteristic, and (*ii*) its capacity for suppressing noise in measured data.

There are many ways to discretize the various partial differential equation (PDE) or integral equation operators which can be used to formulate the electromagnetic scattering problem. Starting with a PDE formulation, the finite-element method is a powerful and flexible discretization technique which has been coupled with GNI in the past e.g., [10]. In this technique the unknown contrast is represented on a dual FEM mesh, different from the mesh used in the FEM solution of the electromagnetic field problem, and interpolation is used between the two meshes. Recently, it has been shown how FEM can be used with the CSI method [11]. Unlike other CSI implementations, FEM-CSI offers several benefits that include: (*i*) performing the inversion on an arbitrary irregular grid of triangles, (*ii*) incorporating an inhomogeneous medium as a background reference, (*iii*) controlling the density of the mesh adaptively within the inversion domain, and (*iv*) easily incorporating radiating or arbitrarily-shaped conductive boundaries surrounding the MWT setup.

In this communication, a novel technique for incorporating multiplicative regularization in the FEM-CSI algorithm is introduced. In typical MR-CSI inversion algorithms, including the finite-difference CSI method reported in [4], the unknown variables are located on a uniform grid of rectangular cells [3], [7]. In such methods, finite-difference approximations for the gradient and divergence operators used in multiplicative regularization can be easily applied. When FEM is used to discretize the electromagnetic field problem, the unknown variables are located on the nodes of an irregular triangular mesh; thus applying MR using finite-differences becomes difficult. Herein a new technique is introduced to perform the gradient and divergence operators on a triangular mesh. The communication begins by describing the formulation of the MWT problem which is used, followed by a brief overview of the FEM-CSI algorithm. Next, the method for applying MR to the triangular mesh is described. To test the algorithm, it is used to invert experimental data and its reconstructions are compared with those from FEM-CSI, without MR.

II. Problem Statement

Consider an imaging domain $\mathcal{D}$ within the problem domain Ω of an MWT setup. The domain Ω is enclosed by boundary Γ. An unknown isotropic, nonmagnetic OI is located in $\mathcal{D}$ and is surrounded by a background medium of known electrical properties. The complex relative permittivity of the OI is $\epsilon_r(\boldsymbol{r})$, where $\boldsymbol{r}$ is a 2D position vector. The corresponding electric contrast is defined as $\chi(\boldsymbol{r}) \triangleq (\epsilon_r(\boldsymbol{r}) - \epsilon_b(\boldsymbol{r}))/\epsilon_b(\boldsymbol{r})$ where $\epsilon_b(\boldsymbol{r})$ is the background complex relative permittivity ($\chi(\boldsymbol{r}) = 0$ for $\boldsymbol{r} \notin \mathcal{D}$), which may be inhomogeneous. The same configuration and notation as given in [11] is used.

The imaging domain $\mathcal{D}$ is illuminated by a harmonic TM electromagnetic field produced by one of $\mathcal{T}$ point sources, producing incident field E_t^{inc} when there is no OI in $\mathcal{D}$. With the OI in $\mathcal{D}$ the total field E_t for the same source t is measured at points located on a measurement surface $\mathcal{S}$. The scattered electric field, defined by $E_t^{\mathrm{sct}} \triangleq E_t - E_t^{\mathrm{inc}}$, satisfies the scalar Helmholtz equation

$$\nabla^2 E_t^{\mathrm{sct}}(\boldsymbol{r}) + k_b^2(\boldsymbol{r}) E_t^{\mathrm{sct}}(\boldsymbol{r}) = -k_b^2(\boldsymbol{r}) w_t(\boldsymbol{r}) \tag{1}$$

where $k_b(\boldsymbol{r}) = \omega\sqrt{\mu_0 \epsilon_0 \epsilon_b(\boldsymbol{r})}$ is the background wavenumber, and $w_t(\boldsymbol{r}) \triangleq \chi(\boldsymbol{r}) E_t(\boldsymbol{r})$ is the contrast source.

When the MWT setup is enclosed within a conductive-enclosure, homogeneous Dirichlet boundary conditions (BCs) are applied to the total field on Γ, corresponding to inhomogeneous BCs for the scattered field. For unbounded-region problems Sommerfeld radiating BCs are imposed on the boundary.

The boundary-value problem (BVP) defined by the second-order PDE (1) and the boundary conditions is solved using FEM with the Rayleigh-Ritz formulation [12]. Thus, the problem domain (Ω) is divided into a mesh of triangular elements constituted by a total number of N nodes. At each node, linear-basis functions are specified whose parameters are dependent only on the geometry of the mesh. The discretization of (1) using FEM produces a matrix equation as detailed in [11]. This equation can be solved efficiently as the associated matrices

Manuscript received January 14, 2011; accepted February 23, 2011. Date of publication July 12, 2011; date of current version September 02, 2011. This work was supported in part by the Natural Sciences and Engineering Research Council of Canada, the University of Manitoba Graduate Fellowship, the Government of Manitoba Graduate Scholarship, and in part by the Gordon P. Osler Award.

The authors are with the Department of Electrical and Computer Engineering, University of Manitoba, Winnipeg, MB R3T5V6 Canada (e-mail: Joe_LoVetri@umanitoba.ca).

Color versions of one or more of the figures in this communication are available online at http://ieeexplore.ieee.org.

Digital Object Identifier 10.1109/TAP.2011.2161564

are sparse, symmetric and independent of OI and the location of transmitter t.

III. Inversion Algorithm

A. Contrast Source Inversion

The CSI objective functional, which is to be minimized, is formulated with respect to the contrast sources, w_t, and the contrast, χ, variables and is constructed as the sum of the normalized data-error and normalized domain-error functionals [11], [13]. It is written as

$$\begin{aligned}\mathcal{F}^{\mathrm{CSI}}(\chi, w_t) &= \mathcal{F}^{\mathcal{S}}(w_t) + \mathcal{F}^{\mathcal{D}}(\chi, w_t) \\ &= \frac{\sum_t \|f_t - \boldsymbol{\mathcal{M}}_{\mathcal{S}} \boldsymbol{\mathcal{L}}[w_t]\|_{\mathcal{S}}^2}{\sum_t \|f_t\|_{\mathcal{S}}^2} \\ &\quad + \frac{\sum_t \left\|\chi \odot E_t^{\mathrm{inc}} - w_t + \chi \odot \boldsymbol{\mathcal{M}}_{\mathcal{D}} \boldsymbol{\mathcal{L}}[w_t]\right\|_{\mathcal{D}}^2}{\sum_t \|\chi \odot E_t^{\mathrm{inc}}\|_{\mathcal{D}}^2}. \quad (2)\end{aligned}$$

Here $f_t \in \mathbb{C}^R$ holds the measured scattered field data at the R receiver locations for each transmitter, $\chi \in \mathbb{C}^I$ is the vector of contrast nodal values for nodes located inside $\mathcal{D}$, and $E_t^{\mathrm{inc}} \in \mathbb{C}^I$ is the vector of incident field corresponding to transmitter t for nodes inside $\mathcal{D}$. The notation $a \odot b$ denotes the Hadamard (i.e., element-wise) product.

In addition, $\boldsymbol{\mathcal{L}} \in \mathbb{C}^{N \times I}$ is the inverse of the FEM matrix operator and it transforms contrast source variables $w_t \in \mathbb{C}^I$ in $\mathcal{D}$ to N nodal scattered field values, the operator $\boldsymbol{\mathcal{M}}_{\mathcal{S}} \in \mathbb{C}^{R \times N}$ transforms field values from N nodes in Ω to R receiver locations on the measurement surface $\mathcal{S}$ and the operator $\boldsymbol{\mathcal{M}}_{\mathcal{D}} \in \mathbb{R}^{I \times N}$ transforms values from N nodes in Ω to I points located inside the imaging domain $\mathcal{D}$

The CSI objective functional $\mathcal{F}^{\mathrm{CSI}}(\chi, w_t)$ is minimized by updating the contrast source w_t and the contrast χ variables sequentially.

First, with the contrast variables χ held constant, the contrast source variables w_t are updated by a conjugate-gradient (CG) method with Polak-Ribière search directions. Next, assuming the contrast source variables w_t are constant, the functional becomes quadratic in the contrast variables χ; therefore, the contrast variables are updated analytically.

The initial guess for the FEM-CSI algorithm, $w_{t,0}$, is not set to zero, and is taken to be the minimizer of the data-error functional $\mathcal{F}^{\mathcal{S}}(w_t)$ after one line-minimization in the method of steepest descent. After evaluating $w_{t,0}$, the initial guess for χ is calculated analytically. The initial search directions are set equal to zero.

Due to the use of a differential-based operator (FEM) in CSI, some changes are necessary to the original CSI algorithm. These changes along with details about the FEM-CSI algorithm are detailed in [11].

B. Multiplicatively Regularized FEMCSI

The weighted L_2-norm regularization factor is implemented by introducing a multiplicative term to the CSI objective functional [3], [8]. Thus, the objective functional at the nth iteration becomes

$$\mathcal{F}_n(\chi, w_t) = \mathcal{F}_n^{\mathrm{MR}}(\chi) \times \mathcal{F}^{\mathrm{CSI}}(\chi, w_t) \quad (3)$$

where the regularization term $\mathcal{F}_n^{\mathrm{MR}}(\chi)$ is given by

$$\mathcal{F}_n^{\mathrm{MR}}(\chi) = \int_{\mathcal{D}} b_n^2(\boldsymbol{r}) \left(|\nabla \chi(\boldsymbol{r})|^2 + \delta_n^2\right) d\boldsymbol{r}. \quad (4)$$

Here

$$b_n^2(\boldsymbol{r}) = \frac{1}{A\left(|\nabla \chi_{n-1}(\boldsymbol{r})|^2 + \delta_n^2\right)} \quad (5)$$

where A is the total area of domain $\mathcal{D}$ and $\delta_n^2 = \mathcal{F}^{\mathcal{D}}(\chi_n^{\mathrm{CSI}}, w_{t,n})\, \bar{A}^{-1}$ in which $\bar{A}$ is the mean area of the mesh triangles in $\mathcal{D}$.

Since $\mathcal{F}_n^{\mathrm{MR}}(\chi_{n-1}) = 1$, the update procedure for the contrast source variables w_t remains unchanged; however, this is not the case for the contrast variables χ. After calculating the contrast variables in CSI, they are updated by a CG method using Polak-Ribière search directions as detailed in [7], [8].

C. Spatial Derivatives on a Triangular Mesh

The calculation of the CG search directions in MR-CSI requires the accurate evaluation of the gradient and divergence of the contrast at nodal locations of the arbitrary triangular FEM mesh; this is not as straightforward as when using a uniform rectangular grid. The unknown contrast is represented using linear basis functions with a gradient which is constant over each triangle and is discontinuous between triangles. Thus, the divergence of the gradient at each node is not easily defined. If quadratic elements are used, the gradient would be a linear function over each element but the divergence would still be discontinuous between elements. Thus, some form of averaging is required. The method described here evaluates the divergence at each node by integrating the gradient over a stencil, having the centroids of the triangles associated with that node as the vertices.

The spatial gradient of the contrast can be calculated numerically over each triangle in the mesh using the first-order basis functions. In FEM, the contrast within a triangle m is given by

$$\chi^{(m)}(\boldsymbol{r}) = \sum_{l=1}^{3} \chi_l^{(m)} \lambda_l^{(m)}(\boldsymbol{r}) \quad (6)$$

where l is a local index for each node on triangle m, $\chi_l^{(m)}$ is the contrast value at node l of triangle m, and the first-order linear basis function for node l is

$$\lambda_l^{(m)}(\boldsymbol{r}) = \frac{1}{A^{(m)}} \left(a_l^{(m)} + b_l^{(m)} x + c_l^{(m)} y\right). \quad (7)$$

Here $A^{(m)}$ is the area of triangle m and the coefficients $a_l^{(m)}$, $b_l^{(m)}$ and $c_l^{(m)}$ are dependent on triangle geometry [12].

The spatial gradient of the contrast within triangle m is then calculated as

$$\begin{aligned}\nabla \chi^{(m)} &= \sum_{l=1}^{3} \chi_l^{(m)} \nabla \lambda_l^{(m)}(\boldsymbol{r}) \\ &= \frac{1}{A^{(m)}} \sum_{l=1}^{3} \chi_l^{(m)} \left(b_l^{(m)} \hat{x} + c_l^{(m)} \hat{y}\right) \quad (8)\end{aligned}$$

where $\hat{x}$ and $\hat{y}$ are the Cartesian unit vectors.

The spatial gradient in (8) is used to calculate the coefficients b_n^2 for each triangle in $\mathcal{D}$ and then to evaluate the multiplicative regularization term $\mathcal{F}_n^{\mathrm{MR}}(\chi)$.

To update the contrast variables χ, the gradient g_n^{χ} has to be evaluated at each node in $\mathcal{D}$. For each node i let us define $\zeta_{i,n}$ as follows:

$$\begin{aligned}\zeta_{i,n} &= \nabla \cdot \xi_{i,n} \\ &= \nabla \cdot \left(\xi_{i,n}^x \hat{x} + \xi_{i,n}^y \hat{y}\right) \\ &= \hat{x} \cdot \nabla \xi_{i,n}^x + \hat{y} \cdot \nabla \xi_{i,n}^y \quad (9)\end{aligned}$$

where $\xi_{i,n} = b_{i,n}^2 \nabla \chi_{i,n}$. Since b_n^2 and $\nabla \chi_n$ are calculated for each triangle rather than each node, the spatial divergence in (9) needs to be approximated.

Let us define a region Ω_i around node i as depicted in Fig. 1. The vertices of this region are the centroids of triangles sharing node i. Using vector identities and the divergence theorem, it can be shown that

$$\begin{aligned}\hat{x} \cdot \nabla \xi_{i,n}^x &\approx \langle \hat{x} \cdot \nabla \xi_n^x(\boldsymbol{r}) \rangle_{\Omega_i} \\ &= \frac{1}{A_i} \oint_{\Gamma_i} \xi_n^x(\boldsymbol{r}) \hat{x} \cdot \hat{n}\, dl_i \quad (10)\end{aligned}$$

where $\langle \cdot \rangle_{\Omega_i}$ denotes the average value over region Ω_i, A_i is the area of Ω_i, Γ_i is the contour (boundary) of Ω_i and $\hat{n}$ is outward normal vector to Γ_i.

Similarly the second term in (9) is approximated as

$$\hat{y} \cdot \nabla \xi_{i,n}^y \approx \frac{1}{A_i} \oint_{\Gamma_i} \xi_n^y(\boldsymbol{r}) \hat{y} \cdot \hat{n}\, dl_i. \quad (11)$$

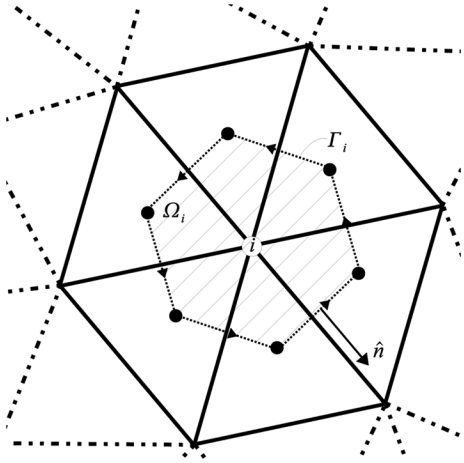

Fig. 1. Region surrounding node $\boldsymbol{i}$ to approximate the spatial divergence. The "●" in the diagram represents the centroid of a triangle.

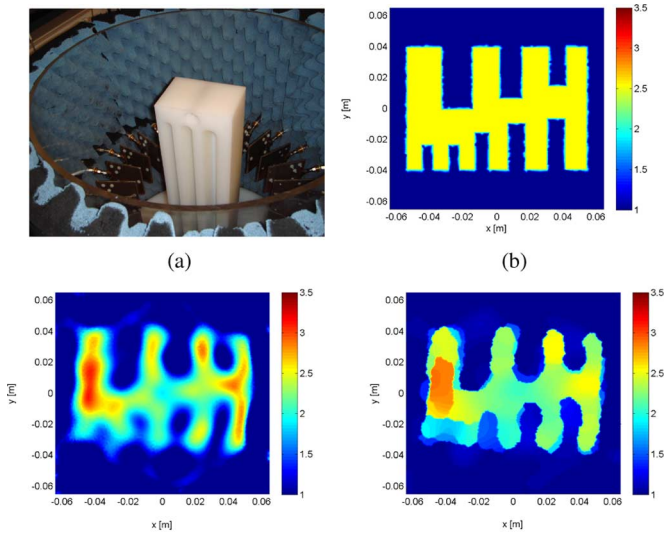

Fig. 2. The "e-phantom" (a) inside the imaging setup, (b) its exact profile at $\boldsymbol{f = 5}$ GHz, and the reconstruction results using (c) FEM-CSI and (d) MR-FEMCSI.

Since the values of $\xi_n(\boldsymbol{r})$ are known at the vertices of region Ω_i, the line integrals in (10) and (11) are evaluated numerically. Here the trapezoidal rule is used to calculate the integral over each segment in region Ω_i.

IV. Experimental Results

The MR-FEMCSI algorithm is tested by inverting an experimental dataset collected using our air-filled MWT system. A full description of the MWT imaging system utilized here is outlined in [14]. This system is air-filled with 24 Vivaldi antennas used as transmitters and receivers. The Vivaldi antennas are evenly distributed on a circle of radius 0.22 m. For each transmitting antenna, 23 measurements are collected (total number of measurements for a dataset is $23 \times 24 = 522$). The measured data are calibrated using the procedure described in [14]. The experimental dataset is acquired at a frequency $f = 5$ GHz.

An "e-phantom" with multiple concave features is used as a target. A side-view of the actual target is shown in Fig. 2(a), while the exact permittivity profile is depicted in Fig. 2(b). The "e-phantom" is constructed of ultrahigh-molecular-weight (UHMW) polyethylene which is a lossless material of relative permittivity $\epsilon_r = 2.3$ [15]. The inversion domain $\mathcal{D}$ is selected to be a square centered in the problem domain Ω with side length equal to 0.13 m.

The computational complexity of the inversion algorithm is reduced by adapting the inversion mesh such that the mesh is denser within the imaging domain $\mathcal{D}$ in comparison to outside $\mathcal{D}$. This results in the number of unknowns in $\mathcal{D}$ to be 13706 nodes, while the total number of nodes N in problem domain Ω is 19390. The ability to control the mesh density demonstrates an advantage of FEM-CSI in comparison to other CSI formulations.

The inversion algorithm is allowed to run for 1024 iterations to ensure convergence. In addition, after each iteration the inversion results are constrained to lie within the region defined by $0 \leq \mathrm{Re}(\epsilon_r) \leq 80$ and $-20 \leq \mathrm{Im}(\epsilon_r) \leq 0$.

The real parts of inversion using FEM-CSI and MR-FEMCSI are shown in Fig. 2(c) and (d) (the imaginary parts are omitted because the background and the target are lossless). Using multiplicative regularization the shape and edges of the target is well reconstructed; however features of the "e-phantom" smaller than 8 mm (approx. $2\lambda/15$, where λ is the free-space wavelength) are not resolved. This result is similar to that obtained using MR-GNI on a uniform grid as reported in [16]. The MR-FEMCSI reconstruction is more homogeneous within the target contour in comparison to the FEM-CSI result; in addition the value of the permittivity is not overshot by MR-FEMCSI.

V. Conclusion

A multiplicatively regularized finite-element method contrast source inversion (MR-FEMCSI) algorithm has been presented and validated for 2D microwave tomography under the TM approximation of the fields. The algorithm retains the advantages of FEM-CSI, such as the ability to invert data on an arbitrary triangular mesh and allowing a non-uniform discretization of the problem domain. The addition of multiplicative regularization adds noise suppression to the inversion and enhances the edges of the reconstructed images while flattening regions of constant contrast. A new technique to calculate the gradient and divergence operators required for multiplicative regularization is outlined which can be used on the unknown contrast variables located on the nodes of such arbitrary triangular meshes. The performance of the algorithm is demonstrated by inverting experimental data.

References

[1] P. Mojabi and J. LoVetri, "Microwave biomedical imaging using the multiplicative regularized Gauss-Newton inversion," *IEEE Antennas Wireless Propag. Lett.*, vol. 8, pp. 645–648, 2009.

[2] P. Mojabi and J. LoVetri, "Overview and classification of some regularization techniques for the Gauss-Newton inversion method applied to inverse scattering problems," *IEEE Antennas Wireless Propag. Lett.*, vol. 8, pp. 645–648, 2009.

[3] A. Abubakar, P. M. van den Berg, and J. J. Mallorqui, "Imaging of biomedical data using a multiplicative regularized contrast source inversion method," *IEEE Trans. Microwave Theory Tech.*, vol. 50, no. 7, pp. 1761–1777, Jul. 2002.

[4] C. Gilmore, A. Abubakar, W. Hu, T. Habashy, and P. van den Berg, "Microwave biomedical data inversion using the finite-difference contrast source inversion method," *IEEE Trans. Antennas Propag.*, vol. 57, no. 5, pp. 1528–1538, May 2009.

[5] P. M. van den Berg and A. Abubakar, "Contrast source inversion method: State of art," *Progr. Electromagn. Res.*, vol. 34, pp. 189–218, 2001.

[6] P. M. van den Berg, A. L. van Broekhoven, and A. Abubakar, "Extended contrast source inversion," *Inverse Prob.* vol. 15, no. 5, p. 1325, 1999 [Online]. Available: http://stacks.iop.org/0266-5611/15/i=5/a=315

[7] P. M. van den Berg, A. Abubakar, and J. Fokkema, "Multiplicative regularization for contrast profile inversion," *Radio Sci.*, vol. 38, no. 2, p. 23 (1–10), 2003.

[8] A. Abubakar, W. Hu, P. van den Berg, and T. Habashy, "A finite-difference contrast source inversion method," *Inverse Prob.*, vol. 24, p. 065004 (17 pp), 2008.

[9] C. Gilmore and J. LoVetri, "Enhancement of microwave tomography through the use of electrically conducting enclosures," *Inverse Prob.* vol. 24, no. 3, p. 035008, 2008 [Online]. Available: http://stacks.iop.org/0266-5611/24/i=3/a=035008

[10] K. D. Paulsen, P. Meaney, M. Moskowitz, and J. S. , Jr., "A dual mesh scheme for finite element based reconstruction algorithms," *IEEE Trans. Med. Imaging*, vol. 14, no. 3, pp. 504–514, Sep. 1995.
[11] A. Zakaria, C. Gilmore, and J. LoVetri, "Finite-element contrast source inversion method for microwave imaging," *Inverse Prob.* vol. 26, no. 11, p. 115010, 2010 [Online]. Available: http://stacks.iop.org/0266-5611/26/i=11/a=115010
[12] J. Jin, *The Finite Element Method in Electromagnetics*. New York: Wiley, 2002.
[13] P. M. van den Berg and R. E. Kleinman, "A contrast source inversion method," *Inverse Prob.* vol. 13, no. 6.
[14] C. Gilmore, P. Mojabi, A. Zakaria, M. Ostadrahimi, C. Kaye, S. Noghanian, L. Shafai, S. Pistorius, and J. LoVetri, "A wideband microwave tomography system with a novel frequency selection procedure," *IEEE Trans. Biomed. Engrg.*, vol. 57, no. 4, pp. 894–904, Apr. 2010.
[15] W. S. Bigelow and E. G. Farr, "Impulse propagation measurements of the dielectric properties of several polymer resins," Measurement Notes, Note 55, 1999, pp. 1–52.
[16] C. Gilmore, P. Mojabi, A. Zakaria, S. Pistorius, and J. LoVetri, "On super-resolution with an experimental microwave tomography system," *IEEE Antennas Wireless Propag. Lett.*, vol. 9, pp. 393–396, 2010.

Statistical Characterization of Medium Wave Spatial Variability Due to Urban Factors

Unai Gil, Ivan Peña, David Guerra, David de la Vega, Pablo Angueira, and Juan Luis Ordiales

***Abstract*—The recently developed digital radio systems for the medium wave (MW) band require accurate field strength prediction methods for coverage calculi. Traditional prediction methods do not consider the influence of urban factors on MW ground-wave propagation. This influence causes signal strength time and spatial variability which in turn, provoke drop-outs below reception threshold values. In this letter the ground-wave spatial variability is statistically analyzed in urban environments by means of empirical data from four extensive field trials. The experiments were carried out in different urban environments and at different frequencies of the MW band. Prior to the analysis, long-term and short-term components of the signal were separated by means of the generalized Lee method (GLM). The results show the attenuation caused by different urban factors. These attenuation values should be added to the signal strength predicted median values in order to ensure correct reception.**

***Index Terms*—Coverage prediction, medium wave (MW) , propagation models, signal variability, urban environments.**

I. Introduction

New digital radio broadcasting systems [1] in the medium wave (MW) band are to be fully deployed shortly. Network planning of traditional broadcasting systems in MW was based on the field strength prediction curves provided by ITU-R [2]. As the ground-wave is assumed to have no variability, these curves provide only median values [3]. However the experience from different field trials [4] showed that this assumption was optimistic in urban environments. As a consequence, the unforeseen variability could cause the signal strength to decrease below the threshold value.

Up to now, time and spatial variability have been studied in rural areas [4], [5], but only time variability has been dealt with as regards urban environments. Hence, spatial variability in urban environments in the MW band needs to be analyzed [6].

This paper presents the statistical characterization of the signal variability by means of analyzing the attenuation caused by urban factors.

The analysis is based on data which were recorded during four extensive field trials carried out in urban environments.

Each trial included different features and studies for different frequencies, always within the MW band.

First, the field trials and the features of the involved urban environments are described. Second, the methodology for processing the empirical data is explained. Third, the calculated attenuation values are presented. Finally, as a conclusion, the influence of frequency and the features of different kind of urban environments is discussed.

TABLE I
Transmitter Features

Center - Broadcaster	Distance to downtown (km)	Tx Antenna height	Frequency (kHz)	Power (kW)
Arganda (Madrid) - Radio Nacional de España	25	λ/4	1359	4 rms
Iztapalapa (México D.F.) - Radio Educación	13	λ/2	1060	1.25 rms
Kamphur (Delhi) - All India Radio	9	λ/4	666	2.5 rms
Pozuelo (Madrid) - Cadena SER	15	λ/4	1260	12.5 rms
Pozuelo (Madrid) - Cadena SER	15	λ/4	810	25 peak

II. Measurement Campaigns

The data analyzed in this paper was gathered during three measurement campaigns that evaluated digital radio mondiale (DRM) mobile reception in MW. An additional measurement campaign of AM signals was also included in the study. It is important to mention that considering the bandwidths involved, the broadcasted service should not affect signal propagation. The transmission features of these measurement campaigns are summarized in Table I.

As can be seen, data from a complete range of frequencies within the MW band was available. The cities involved are representative of different kinds of urban environments as shown in Table II. In all three cities, the traffic density was very high when the measurements were carried out. In fact, studies in the past identified traffic as an attenuation factor for propagation in the medium wave band [4].

The measurement system was set up in a mobile unit and it was composed of a fully characterized short monopole antenna placed at 3.5 m height [7] and a professional field strength meter [8] that integrated the power within the signal bandwidth. Finally a GPS receiver and a tachometer provided ancillary data related to position, time, speed and distance. These data were captured every 400 ms (the DRM frame duration) and were stored in plain text files. More than 700 km of measurements were recorded during the measurement campaigns of Table I.

Manuscript received August 26, 2010; revised February 22, 2011; accepted February 26, 2011. Date of publication July 12, 2011; date of current version September 02, 2011. This work was supported in part by the Spain Government under Grants TEC2005-06139 and FIT-330301-2007-1 and in part by the Government of the Basque Country This communication has been produced by the Signal and Radio Communications Group of The University of the Basque Country. This work is due to a cooperative partnership between the DRM Consortium and Cadena SER (Spain), All India Radio (India) and Radio Educación (Mexico) broadcasters. Deutsche Welle, TDF, Radio Netherlands and Fraunhofer Institute of Erlangen, Himalaya, Thomson, Transradio and Hitachi Kokusai have generously donated all the measurement equipment for these field trials.

The authors are with the Electronics and Telecommunications Department, University of the Basque Country UPV/EHU, Bilbao, Bizkaia, Spain (e-mail: daviz@bips78.bi.ehu.es).

Digital Object Identifier 10.1109/TAP.2011.2161550